

Steady Rayleigh–Bénard convection between no-slip boundaries

Baole Wen^{1†}, David Goluskin^{2‡}, and Charles R. Doering^{1,3,4}

¹Department of Mathematics, University of Michigan, Ann Arbor, MI 48109-1043, USA

²Department of Mathematics & Statistics, University of Victoria, Victoria, BC, V8P 5C2, Canada

³Department of Physics, University of Michigan, Ann Arbor, MI 48109-1040, USA

⁴Center for the Study of Complex Systems, University of Michigan, Ann Arbor, MI 48109-1042, USA

(Received xx; revised xx; accepted xx)

The central open question about Rayleigh–Bénard convection—buoyancy-driven flow in a fluid layer heated from below and cooled from above—is how vertical heat flux depends on the imposed temperature gradient in the strongly nonlinear regime where the flows are typically turbulent. The quantitative challenge is to determine how the Nusselt number Nu depends on the Rayleigh number Ra in the $Ra \rightarrow \infty$ limit for fluids of fixed finite Prandtl number Pr in fixed spatial domains. Laboratory experiments, numerical simulations, and analysis of Rayleigh’s mathematical model have yet to rule out either of the proposed ‘classical’ $Nu \sim Ra^{1/3}$ or ‘ultimate’ $Nu \sim Ra^{1/2}$ asymptotic scaling theories. Among the many solutions of the equations of motion at high Ra are steady convection rolls that are dynamically unstable but share features of the turbulent attractor. We have computed these steady solutions for Ra up to 10^{14} with $Pr = 1$ and various horizontal periods. By choosing the horizontal period of these rolls at each Ra to maximize Nu , we find that steady convection rolls achieve classical asymptotic scaling. Moreover, they transport more heat than turbulent convection in experiments or simulations at comparable parameters. If heat transport in turbulent convection continues to be dominated by heat transport in steady rolls as $Ra \rightarrow \infty$, it cannot achieve the ultimate scaling.

Key words: convection, coherent structure, heat transport

1. Introduction

Rayleigh–Bénard convection (RBC) is the buoyancy-driven flow in a fluid layer heated from below and cooled from above in the presence of gravity. The emergent convective flow enhances heat flux from the warm bottom boundary to the cool top boundary beyond the conductive flux from diffusion alone. This dimensionless enhancement factor—the ratio of bulk-averaged vertical heat flux from both conduction and convection to the flux from conduction alone—defines the Nusselt number Nu . In Rayleigh’s mathematical model (Rayleigh 1916) Nu depends on several dimensionless quantities characterizing the problem at hand: (i) what we now call the Rayleigh number Ra , which is proportional to the imposed temperature drop across the layer, (ii) the fluid’s Prandtl number Pr , which

† Email address for correspondence: baolew@umich.edu

‡ Email address for correspondence: goluskin@uvic.ca

is the ratio of kinematic viscosity to thermal diffusivity, and (iii) details of the spatial domain, often captured by an aspect ratio Γ that is a ratio of a horizontal length scale to the vertical layer height.

Convection is *coherent* at Ra values not too far above the critical value Ra_c beyond which the conductive no-flow state is linearly unstable. By coherent we mean flows with few scales present; spatial scales might include a horizontal period and the vertical thickness of boundary layers, and temporally the flow may be steady or time-periodic. Meanwhile, convection is *turbulent* at the large Ra values pertinent to many engineering and scientific applications. Turbulent flows are complex and contain a range of spatial and temporal scales and, in the present context, have thermal and viscous boundary layers at the top and bottom boundaries from which thermal plumes emerge and mix the bulk. In a given domain it is expected that a scaling of Nu with respect to both Pr and Ra will emerge in the $Ra \rightarrow \infty$ limit (Kadanoff 2001).

After nearly a century of increasingly sophisticated mathematical analysis, increasingly resolved direct numerical simulations (DNS), and increasingly refined laboratory experiments, two quantitatively distinct conjectures remain in contention for the heat transport scaling law at large Ra (Chillà & Schumacher 2012; Doering 2020). The two conjectures follow from heuristic physical arguments that both seem plausible but give incompatible predictions: the ‘classical’ scaling $Nu \sim Pr^0 Ra^{1/3}$ and the ‘ultimate’ scaling $Nu \sim Pr^{1/2} Ra^{1/2}$, with the latter sometimes including logarithmic-in- Ra modifications.

For RBC between flat, no-slip, isothermal boundaries, rigorous analysis of the governing equations has yielded upper bounds of the form $Nu \leq \mathcal{O}(Ra^{1/2})$ uniformly in Pr and Γ (Howard 1963; Doering & Constantin 1996), but this still allows for either classical or ultimate scaling. Upper bounds that rule out ultimate scaling by being asymptotically smaller than $\mathcal{O}(Ra^{1/2})$ have been derived in the limit of infinite Pr (Doering *et al.* 2006; Otto & Seis 2011; Whitehead & Doering 2012) and for two-dimensional convection between stress-free boundaries (Whitehead & Doering 2011). For the no-slip boundaries relevant to experiments, however, it remains an open question whether an upper bound asymptotically smaller than $Ra^{1/2}$ is possible.

In view of the problem’s stubbornness, a new strategy is called for to determine—or at least to bound— Nu as a function of Ra , Pr , and Γ . Toward that end we have undertaken an indirect approach consisting of two parts. The first part is to study coherent flows for which one can reasonably hope to determine asymptotic heat transport, and the second part is to investigate how transport by those coherent flows compares with transport by turbulent convection. The simplest coherent flows are steady—i.e., time-independent—solutions of the equations of motion. Many such states exist, although they are generally unstable at large Ra . We focus on what might be called the simplest type of steady states: two-dimensional convection rolls like the counter-rotating pairs shown in figure 1(*a*, *b*). In horizontally periodic or infinite domains in two or three dimensions, such rolls bifurcate supercritically from the conductive state in the linear instability identified by Rayleigh (1916). A roll pair of any width-to-height aspect ratio Γ admitted by the domain exists for sufficiently large Ra .

For steady rolls, the dependence of Nu on the parameters (Γ, Pr, Ra) at *asymptotically large* Ra is accessible to computation. As for whether heat transport by steady rolls can be connected to transport by turbulence, there are several reasons for optimism. Relationships between turbulent attractors and the unstable coherent states embedded therein have been established in models of wall-bounded shear flows (Graham & Floryan 2021), where particular steady states, traveling waves, and time-periodic states have been found that closely reflect turbulent flows in terms of integral quantities as well as particular flow structures. Analogous study of RBC began only recently but indeed suggests that

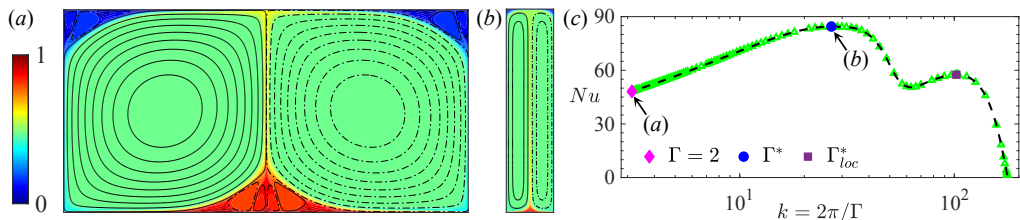


Figure 1: Steady convection rolls at $Ra = 10^9$ and $Pr = 1$ with (a) $\Gamma = 2$ and (b) the value $\Gamma^* \approx 0.235$ that maximizes Nu at these values of Ra and Pr . Color indicates temperature, and streamlines are shown for counterclockwise (solid) and clockwise (dash-dotted) motions. (c) Dependence of Nu on the horizontal wavenumber $k = 2\pi/\Gamma$ found by computing steady rolls of various aspect ratios (\triangle). Highlighted points are the two Γ shown in panels (a) and (b) along with the value $\Gamma_{loc}^* \approx 0.0614$ that locally maximizes $Nu(\Gamma)$. Cubic spline interpolation (---) is used to find Γ^* and Γ_{loc}^* precisely.

certain steady states capture qualitative aspects of turbulent convection (Waleffe *et al.* 2015; Sondak *et al.* 2015; Kooloth *et al.* 2021; Motoki *et al.* 2021). Our findings add to this evidence. The desire to understand and perhaps strengthen the mathematical bound $Nu \leq \mathcal{O}(Ra^{1/2})$ is further motivation for studying unstable states since bounds apply to all solutions of the governing equations regardless of stability. It is an open question whether *any* solutions can achieve ultimate scaling, let alone turbulent solutions.

Here we report numerical computations of steady convection rolls for a $Pr = 1$ fluid contained between no-slip isothermal top and bottom boundaries. We reach sufficiently large Ra values to convincingly reveal several asymptotic scalings of Nu , depending on the horizontal periods of the rolls. These are the first clearly asymptotic scalings found for any type of flow—steady, turbulent, or otherwise—for RBC in the no-slip case. Notably, the largest heat transport among steady rolls of all horizontal periods displays the classical $Nu \sim Ra^{1/3}$ scaling. We further observe that Nu for these steady rolls is *larger* than turbulent Nu from all laboratory experiments and two- or three-dimensional (2D or 3D) simulations at comparable parameters. This observation supports the conjecture that steady states maximize Nu among all stable or unstable flows, as was recently verified for a truncated model of RBC (Olson *et al.* 2021) using methods that are not yet applicable to the full governing equations. If steady-roll transport continues to dominate turbulent transport as $Ra \rightarrow \infty$, then our finding of classical scaling for steady rolls would rule out ultimate scaling of turbulent convection.

The asymptotic scaling of steady rolls is already known in the case of *stress-free* velocity conditions at the top and bottom boundaries, which were considered for mathematical convenience in Rayleigh’s original work. In that case $Nu \sim Ra^{1/3}$ as $Ra \rightarrow \infty$ at fixed Pr and Γ , and the aspect ratio of the roll pair maximizing Nu at each Ra and Pr approaches $\Gamma \approx 1.9$ (Chini & Cox 2009; Wen *et al.* 2020). Recent computations of steady rolls in the *no-slip* case for pre-asymptotic Ra values up to 10^9 revealed significant differences from the stress-free problem (Waleffe *et al.* 2015; Sondak *et al.* 2015). The dependence $Nu(\Gamma)$ for no-slip rolls at fixed Ra and Pr can have multiple local maxima, as shown in figure 1(c), and the aspect ratio Γ^* that globally maximizes $Nu(\Gamma)$ approaches zero rather than a constant as $Ra \rightarrow \infty$. Steady rolls of Nu -maximizing aspect ratios Γ^* were reported in Sondak *et al.* (2015) for $Ra \in [5 \times 10^6, 3 \times 10^8]$ at $Pr = 1$, yielding fits of $\Gamma^* \sim Ra^{-0.217}$ and $Nu(\Gamma^*) \sim Ra^{0.31}$. This heat transport scaling is faster than with Γ fixed: computations in Waleffe *et al.* (2015) for $Ra \in [5 \times 10^5, 5 \times 10^6]$ at $Pr = 7$ with

$\Gamma = 2$ fixed yield the fit $Nu \sim Ra^{0.28}$. These best-fit scaling exponents are, however, not asymptotic.

Steady convection rolls are dynamically unstable at large Ra and cannot be found by standard time integration, so we employed a purpose-written code that iteratively solves the time-independent equations. We computed rolls with $\Gamma = 2$ fixed for $Ra \lesssim 2 \times 10^{10}$ and with the parameter-dependent aspect ratios Γ^* and Γ_{loc}^* (cf. figure 1) that globally and locally maximize $Nu(\Gamma)$, respectively, for $Ra \leq 10^{14}$. These Ra values are evidently large enough to reach asymptotia: the results reported below strongly suggest that fixed- Γ rolls asymptotically transport heat like $Nu \sim Ra^{1/4}$ while the ever-narrowing rolls of aspect ratio Γ^* achieve the classical $Nu \sim Ra^{1/3}$ scaling.

2. Computation of steady-convection-roll solutions

Following Rayleigh (1916), we model RBC using the Boussinesq approximation to the Navier–Stokes equations with constant kinematic viscosity ν , thermal diffusivity κ , and coefficient of thermal expansion α . We nondimensionalize lengths by the layer height h , temperatures by the fixed difference Δ between the boundaries, velocities by the free-fall scale $U_f = \sqrt{g\alpha h\Delta}$, and time by the free-fall time h/U_f . Calling the horizontal coordinate x and the vertical coordinate z , the gravitational acceleration of magnitude g is in the $-\hat{\mathbf{z}}$ direction. The evolution equations governing the dimensionless velocity vector $\mathbf{u} = (u, w)$, temperature T , and pressure p are then

$$\partial_t \mathbf{u} + \mathbf{u} \cdot \nabla \mathbf{u} = -\nabla p + (Pr/Ra)^{1/2} \nabla^2 \mathbf{u} + T \hat{\mathbf{z}}, \quad (2.1a)$$

$$\nabla \cdot \mathbf{u} = 0, \quad (2.1b)$$

$$\partial_t T + \mathbf{u} \cdot \nabla T = (PrRa)^{-1/2} \nabla^2 T, \quad (2.1c)$$

where

$$Ra = \frac{g\alpha h^3 \Delta}{\kappa \nu} \quad \text{and} \quad Pr = \frac{\nu}{\kappa}. \quad (2.2a,b)$$

The dimensionless spatial domain is $(x, z) \in [0, \Gamma] \times [0, 1]$, and all variables are horizontally periodic. The top and bottom boundaries are isothermal with $T = 0$ and $T = 1$, respectively, while no-slip conditions require \mathbf{u} to vanish on both boundaries. The conductive state $(\mathbf{u}, T) = (\mathbf{0}, 1 - z)$ becomes unstable when Ra increases past the critical value $Ra_c \approx 1708$ (Jeffreys 1928), at which a roll pair with horizontal period $\Gamma \approx 2.016$ bifurcates supercritically. As $Ra \rightarrow \infty$ the horizontal period of the narrowest marginally stable roll pair decreases as $\mathcal{O}(Ra^{-1/4})$, while the horizontal period of the fastest-growing linearly unstable mode decreases more slowly as $\mathcal{O}(Ra^{-1/8})$.

In terms of the dimensionless solutions to (2.1), the Nusselt number is

$$Nu = 1 + (PrRa)^{1/2} \langle wT \rangle, \quad (2.3)$$

where $\langle \cdot \rangle$ denotes an average over the spatial domain and infinite time. For steady states no time average is needed.

To compute rolls at Ra values large enough to reach the asymptotic regime we developed a numerical scheme by adapting the approach of Wen *et al.* (2020) and Wen & Chini (2018) to the case of no-slip boundary conditions. In these numerics the temperature is represented using the deviation θ from the conductive profile, meaning $T = 1 - z + \theta$, and the velocity is represented using a stream function ψ , where $\mathbf{u} = \partial_z \psi \hat{\mathbf{x}} - \partial_x \psi \hat{\mathbf{z}}$ so that the (negative) scalar vorticity is $\omega = \partial_x w - \partial_z u = -\nabla^2 \psi$.

In terms of these variables, steady ($\partial_t = 0$) solutions of (2.1) satisfy

$$\partial_z \psi \partial_x \omega - \partial_x \psi \partial_z \omega = (Pr/Ra)^{1/2} \nabla^2 \omega + \partial_x \theta, \quad (2.4a)$$

$$\nabla^2 \psi = -\omega, \quad (2.4b)$$

$$\partial_z \psi \partial_x \theta - \partial_x \psi \partial_z \theta = -\partial_x \psi + (PrRa)^{-1/2} \nabla^2 \theta \quad (2.4c)$$

with fixed-temperature and no-slip boundary conditions,

$$\theta|_{z=0,1} = 0, \quad \psi|_{z=0,1} = 0, \quad \text{and} \quad \partial_z \psi|_{z=0,1} = 0. \quad (2.5a,b,c)$$

To compute solutions of the time-independent equations (2.4) and (2.5) by an iterative method, we do not need to impose all boundary conditions precisely on each iteration—the conditions need to hold only for the converged solution. Thus we do not impose (2.5c) exactly, instead using approximate boundary conditions on ω for equation (2.4a). These are derived by Taylor expanding ψ about the top and bottom boundaries to find

$$\psi|_{z=1-\delta} = \psi|_{z=1} - \partial_z \psi|_{z=1} \delta + \partial_z^2 \psi|_{z=1} \frac{\delta^2}{2} - \partial_z^3 \psi|_{z=1} \frac{\delta^3}{6} + \mathcal{O}(\delta^4), \quad (2.6a)$$

$$\psi|_{z=\delta} = \psi|_{z=0} + \partial_z \psi|_{z=0} \delta + \partial_z^2 \psi|_{z=0} \frac{\delta^2}{2} + \partial_z^3 \psi|_{z=0} \frac{\delta^3}{6} + \mathcal{O}(\delta^4), \quad (2.6b)$$

where $\delta > 0$ is small. Combining equations (2.4b) with (2.5b,c) and neglecting $\mathcal{O}(\delta^4)$ terms in (2.6) give the approximate boundary conditions,

$$\partial_z \omega|_{z=1} - \frac{3}{\delta} \omega|_{z=1} - \frac{6}{\delta^3} \psi|_{z=1-\delta} = 0, \quad -\partial_z \omega|_{z=0} - \frac{3}{\delta} \omega|_{z=0} - \frac{6}{\delta^3} \psi|_{z=\delta} = 0. \quad (2.7a,b)$$

In computations we set δ to be the distance between the boundary and the first interior mesh point.

The time-independent equations (2.4) are solved numerically subject to boundary conditions (2.5a,b) and (2.7) using a Newton–GMRES (generalized minimal residual) iterative scheme. The spatial discretization is spectral, using a Fourier series in x and a Chebyshev collocation method in z (Trefethen 2000). All of our computations had at least 20 collocation points in the viscous and thermal boundary layers. At Ra just above the linear instability, iterations starting from the unstable eigenmode converge to the steady rolls we seek. At larger Ra , already-computed steady rolls from nearby Ra and Γ values were used as the initial iterate. Every 2 to 4 Newton iterations, we change the boundary values of the iterate to match the $\partial_z \psi = 0$ boundary condition exactly. Prior to convergence this makes the boundary values slightly inconsistent with the governing equations, but the converged solutions satisfy the equations and the no-slip boundary conditions to high precision. Newton iterations were carried out until the Lebesgue L^2 -norm of the residual of the governing steady equations had a relative magnitude less than 10^{-10} . To accurately locate Γ^* and Γ_{loc}^* , rolls were computed at several nearby Γ , and then $Nu(\Gamma)$ was interpolated with cubic splines like those in figure 1(c). Details of computational results, including resolutions used, are included in the supplementary material.

3. Results

We computed steady $Pr = 1$ rolls for aspect ratios Γ encompassing the three distinguished values indicated by figure 1(c): the fixed value $\Gamma = 2$ and the Ra -dependent values Γ^* and Γ_{loc}^* that globally and locally maximize Nu over Γ . As previously observed by Sondak *et al.* (2015), the $Nu(\Gamma)$ curve has a single maximum when Ra is small and

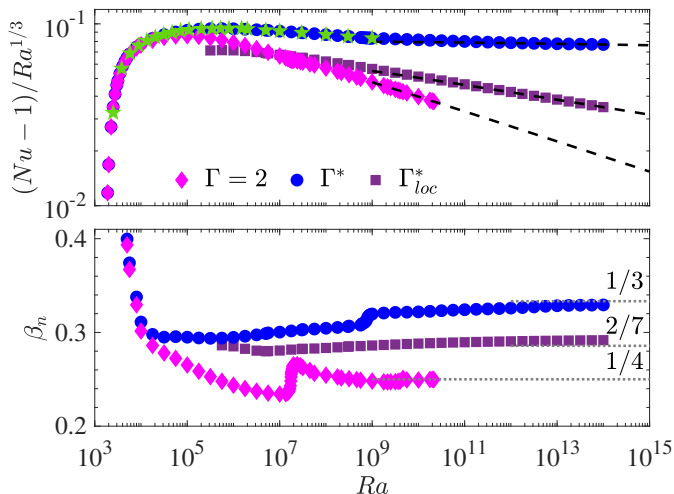


Figure 2: Top: Compensated plot of $Nu - 1$ vs. Ra for steady rolls with $Pr = 1$ and aspect ratios of $\Gamma = 2$, Γ^* , and Γ_{loc}^* , where the Ra -dependent values Γ^* and Γ_{loc}^* are where $Nu(\Gamma)$ has global and local maxima, respectively (cf. figure 1). Values of Nu at Γ^* from Sondak *et al.* (2015) and Waleffe (2020) are also shown (\star). Scaling fits (---) over the last decade of each data set yield exponents of 0.33, 0.29, and 0.25. Bottom: Finite difference approximations of the local scaling exponent $\beta_n = \frac{d(\log Nu)}{d(\log Ra)}$. Exponents of $1/3$, $2/7$, and $1/4$ are shown to guide the eye (-----).

develops a second local maximum at smaller Γ when Ra increases past roughly 2×10^5 . The value of Nu at this second local maximum remains less than the value at the first, so the picture remains as in figure 1(c) with Γ^* on the left and Γ_{loc}^* on the right, in contrast to the $Pr = 10$ and 100 cases (Sondak *et al.* 2015). For most Ra values we did not compute rolls over a full sweep through Γ as in figure 1(c), instead searching over Γ only as needed to locate Γ^* and Γ_{loc}^* . The rest of this section reports Nusselt number and Reynolds number scalings for the computed steady rolls, and the supplementary material provides tabulated data.

3.1. Asymptotic heat transport

Figure 2 shows the dependence of Nu on Ra for steady rolls with aspect ratios $\Gamma = 2$, Γ^* , and Γ_{loc}^* . In the top panel $Nu - 1$ is compensated by $Ra^{1/3}$, so the horizontal line approached by rolls of the Nu -maximizing aspect ratios Γ^* corresponds to classical $1/3$ scaling. The downward slopes of the data for aspect ratios 2 and Γ_{loc}^* correspond to scaling exponents smaller than $1/3$. Values of Nu at Γ^* computed previously for $Ra \leq 10^9$ (Sondak *et al.* 2015; Waleffe 2020) are shown in figure 2 also, and they agree with our computations very precisely—e.g., the $Ra = 10^9$ data point agrees with our value of Nu to within 0.0008%.

The bottom panel of figure 2 shows the Ra -dependent local scaling exponent $\beta_n = \frac{d(\log Nu)}{d(\log Ra)}$ of the Nu - Ra relation for $\Gamma = 2$, Γ^* , and Γ_{loc}^* . This quantity educes small variations not visible in the top panel. In particular, for rolls of aspect ratios Γ^* , the exponent β_n exhibits a small but rapid change just below $Ra = 10^9$, beyond which it smoothly approaches the classical $1/3$ exponent that appears to be the $Ra \rightarrow \infty$ asymptotic behavior. This rapid change seems to coincide with the velocity becoming vertically uniform outside the boundary layers, as reflected in the streamlines of figure 1(b); further

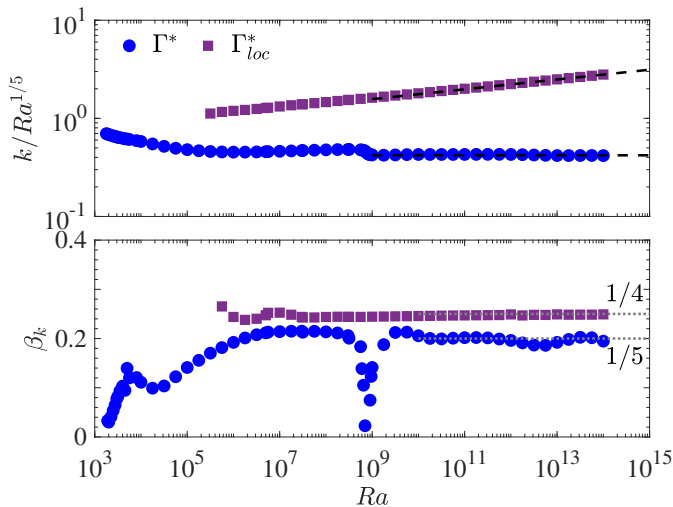


Figure 3: Top: Compensated plot of the fundamental horizontal wavenumber $k = 2\pi/\Gamma$ vs. Ra for the aspect ratios Γ^* and Γ_{loc}^* that maximize $Nu(\Gamma)$ globally and locally, respectively, at $Pr = 1$. Scaling fits (---) to $2\pi/\Gamma^*$ over $Ra \in [10^{10}, 10^{14}]$ and $2\pi/\Gamma_{loc}^*$ over $Ra \in [10^{13}, 10^{14}]$ yield exponents of 0.20 and 0.25, respectively. Bottom: Finite difference approximations of the local exponent $\beta_k = \frac{d(\log k)}{d(\log Ra)}$. The values $1/4$ and $1/5$ (.....) agree with the scaling fit exponents to two digits.

details of the rolls' structure will be reported elsewhere. Rolls with $\Gamma = 2$ fixed undergo a similarly rapid change around $Ra \approx 2 \times 10^7$ and then approach $Nu \sim Ra^{1/4}$ scaling that appears to be asymptotic. Rolls of aspect ratio Γ_{loc}^* show intermediate Nu scaling whose best-fit exponent over the last decade of data is 0.29.

The top panel of figure 3 shows the Ra -dependence of the wavenumber $k = 2\pi/\Gamma$ for Γ^* and Γ_{loc}^* , compensated by $Ra^{1/5}$. The compensated wavenumbers for Γ^* approach a horizontal line, suggesting that the Nu -maximizing rolls narrow according to the power law $\Gamma^* \sim Ra^{-1/5}$. This narrowing of Γ^* is slow relative to the case of RBC in a porous medium, where $\Gamma^* \sim Ra^{-1/2}$ (Wen *et al.* 2015).

The bottom panel of figure 3 shows the Ra -dependence of the local scaling exponent $\beta_k = \frac{d(\log k)}{d(\log Ra)}$. For $k = 2\pi/\Gamma^*$ the local scaling exponent remains close to $1/5$ after the transition around $Ra = 10^9$. For $k = 2\pi/\Gamma_{loc}^*$ the exponent seems to approach $1/4$, suggesting that Γ_{loc}^* has the same $Ra^{-1/4}$ scaling as the narrowest marginally stable mode. Variations in β_k beyond $Ra = 10^{12}$ for Γ^* are evident, but these might be due to numerical imprecision: Nu depends very weakly on Γ around the maximum of $Nu(\Gamma)$, as seen in figure 1(c), so the value of Γ^* cannot be determined nearly as precisely as the value of $Nu(\Gamma^*)$.

3.2. Asymptotic kinetic energy

Another emergent quantity central to RBC is the bulk Reynolds number based on root-mean-squared velocity, which in terms of dimensionless solutions to (2.1) is

$$Re = \left(\frac{Ra}{Pr} \right)^{1/2} \langle |\mathbf{u}|^2 \rangle^{1/2}. \quad (3.1)$$

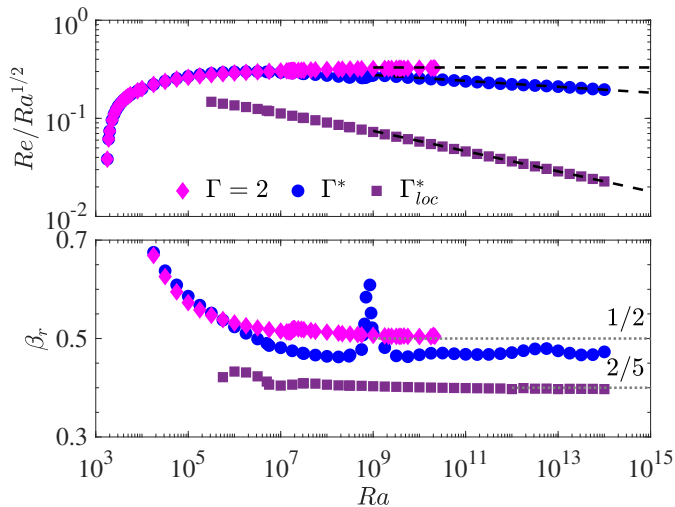


Figure 4: Top: Compensated plot of Re vs. Ra for steady rolls with $Pr = 1$ and aspect ratios $\Gamma = 2$, Γ^* , and Γ_{loc}^* . Scaling fits yield $Re \sim Ra^{0.50}$ for $\Gamma = 2$ and $Re \sim Ra^{0.40}$ for Γ_{loc}^* over the last decade of each data set, and $Re \sim Ra^{0.47}$ for Γ^* over $Ra \in [10^{10}, 10^{14}]$ (---). Bottom: Finite difference approximations to the local exponent $\beta_r = \frac{d(\log Re)}{d(\log Ra)}$. Exponents of $1/2$ and $2/5$ are shown to guide the eye (.....).

Figure 4 depicts the dependence of Re on Ra for the steady rolls of aspect ratios $\Gamma = 2$, Γ^* , and Γ_{loc}^* . The top panel shows Re compensated by $Ra^{1/2}$ while the bottom panel shows the local scaling exponent $\beta_r = \frac{d(\log Re)}{d(\log Ra)}$. Rolls with the fixed aspect ratio $\Gamma = 2$ approach the asymptotic scaling $Re \sim Ra^{1/2}$ that corresponds to the root-mean-squared velocity being proportional to the free-fall velocity U_f . For rolls with Nu -maximizing aspect ratios Γ^* , the scaling fit over $Ra \in [10^{10}, 10^{14}]$ is $Re \sim Ra^{0.47}$, which is quite close to the $Re \sim Ra^{0.46}$ scaling observed in recent 3D direct numerical simulations up to $Ra = 10^{15}$ at $Pr = 1$ in a slender cylinder with a height 10 times its diameter (Iyer *et al.* 2020). For the Γ_{loc}^* rolls the scaling exponent of Re is indistinguishable from $2/5$. The measured exponents (0.50, 0.47, 0.40) are unchanged if Re is defined using the pointwise maximum velocity rather than using the root-mean-squared velocity as in (3.1). All three aspect ratios result in smaller speeds than steady rolls between stress-free boundaries, where $Re \sim Ra^{2/3}$ for any fixed Pr and Γ (Wen *et al.* 2020).

4. Comparison with turbulent convection

To compare heat transport by steady rolls with that by turbulent thermal convection, we compiled Nusselt number data from high- Ra DNS with $Pr = 1$ or 0.7 and laboratory experiments where the estimated Pr is between 0.7 and 1.3 . Figure 5 shows these Nu values compensated by $Ra^{1/3}$, along with Nu values of steady convection rolls at the Nu -maximizing aspect ratios Γ^* . Strikingly, heat transport by the Nu -maximizing 2D steady rolls is *larger* than transport by turbulent convection in all cases.

The turbulent data shown in figure 5, as detailed in the figure caption, include DNS in horizontally periodic 2D and 3D domains, wherein 2D steady rolls solve the equations of motion, as well as 3D DNS and laboratory experiments in cylinders that do not admit 2D rolls. Values of Nu for steady rolls with $\Gamma = 2$ fixed are omitted from figure 5 for

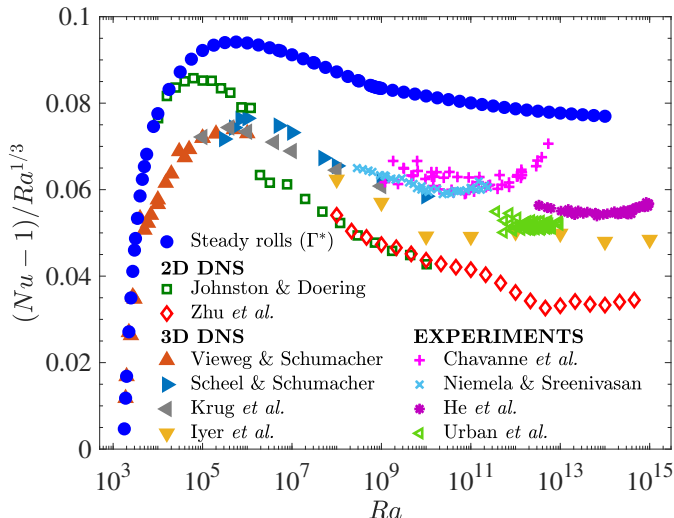


Figure 5: Nu compensated by $Ra^{1/3}$ for steady rolls of Nu -maximizing aspect ratios Γ^* at $Pr = 1$, along with Nu from turbulent 2D and 3D DNS and experiments with estimated $Pr \in [0.7, 1.3]$. For horizontally periodic domains, 2D DNS with $(\Gamma, Pr) = (2, 1)$ were done by Johnston & Doering (2009) and Zhu *et al.* (2018), and 3D DNS with $\Gamma \geq 8$ and $Pr = 1$ were done by Vieweg & Schumacher (2020) and Krug *et al.* (2020). For DNS in cylinders of diameter-to-height ratio Γ_c , Iyer *et al.* (2020) used $(\Gamma_c, Pr) = (0.1, 1)$ and Scheel & Schumacher (2017) used $(\Gamma_c, Pr) = (1, 0.7)$. For laboratory experiments in cylinders, where the plotted data is truncated according to $Pr \in [0.7, 1.3]$, the domains and estimated Pr ranges are $\Gamma_c = 0.5$ and $Pr \in [0.7, 1.3]$ for Chavanne *et al.* (2001), $\Gamma_c = 4$ and $Pr \in [0.7, 1.27]$ for Niemela & Sreenivasan (2006), $\Gamma_c = 0.5$ and $Pr \in [0.79, 0.86]$ for He *et al.* (2012), and $\Gamma_c = 1$ and $Pr \in [0.95, 1.17]$ for Urban *et al.* (2014). Experiments used working fluids of low-temperature helium gas (Chavanne *et al.* 2001; Niemela & Sreenivasan 2006; Urban *et al.* 2014) or sulfur hexafluoride (He *et al.* 2012).

clarity, but they lie below all turbulent values once Ra approximately exceeds 2×10^9 (cf. figure 2), and this gap would only widen at larger Ra if their $Nu \sim Ra^{1/4}$ scaling persists. The laboratory data sets in figure 5 have unavoidably varying Pr values that can be hard to estimate, as well as non-Oberbeck–Boussinesq effects (Urban *et al.* 2011, 2012, 2014). The figure includes only a narrow range of estimated Pr values in order to avoid significant non-Oberbeck–Boussinesq effects. When data over a wider range of estimated Pr is included, a few data points from the experiments of Chavanne *et al.* (2001) lie above the $Nu(\Gamma^*)$ values of steady rolls, as shown in the supplementary material.

Our finding that steady rolls of Nu -maximizing aspect ratios apparently display classical $Nu \sim Ra^{1/3}$ asymptotic scaling does not ineluctably imply anything about turbulent convection. Taking a dynamical systems point of view, however, steady solutions admitted by the domain are fixed points of (2.1), so they and their unstable manifolds are part of the global attractor. Turbulent trajectories may linger near these fixed points and so inherit some quantitative features (Kooloth *et al.* 2021), as has been found for unstable coherent states in shear flows (Nagata 1990; Waleffe 1998; Wedin & Kerswell 2004; Gibson *et al.* 2008; Suri *et al.* 2020; Graham & Floryan 2021). Indeed, figure 5 shows scaling similarities between steady and turbulent convection. Further exploration of the global attractor calls for study of 3D steady flows. Recently computed ‘multi-scale’ 3D steady states (Motoki *et al.* 2021) give larger Nu values than all 2D rolls at moderate Ra , but

their scaling at large Ra is unknown. Simpler 3D steady convection patterns remain to be computed as well. Analytically, it is an open challenge to construct approximations of 2D or 3D steady flows that are asymptotically accurate as $Ra \rightarrow \infty$, as has been done for 2D rolls between stress-free boundaries (Chini & Cox 2009; Wen *et al.* 2020). Such constructions could be used to verify that $Nu \sim Ra^{1/3}$ is indeed the exact asymptotic scaling for the Nu -maximizing rolls we have computed, as well as to determine the precise Re - Ra scaling relations for rolls of both Nu - and Re -maximizing aspect ratios.

More generally, figure 5 highlights the absence of reproducible evidence for ultimate $Nu \sim Ra^{1/2}$ scaling, and it raises the intriguing possibility that *steady* rolls with $Nu \sim Ra^{1/3}$ might transport more heat than turbulent convection as $Ra \rightarrow \infty$. We know of no counterexamples to this hypothesis, including in the case of stress-free boundaries (Wen *et al.* 2020). Heat transport by solutions of (2.1) with no-slip isothermal boundaries has been mathematically proved to be limited by $Nu \leq \mathcal{O}(Ra^{1/2})$ (Howard 1963; Doering & Constantin 1996), but it remains unknown whether any solutions attain the ultimate scaling of this upper bound. One avenue for pursuing a stronger mathematical statement is to study two conjectures suggested by our computations: that steady convection maximizes Nu among all solutions of (2.1) regardless of their stability or time-dependence, and that steady solutions of (2.1) are subject to an upper bound of the form $Nu \leq \mathcal{O}(Ra^{1/3})$. Therefore, although numerically computed flows can never determine $Ra \rightarrow \infty$ scaling definitively, our results suggest a new mathematical approach that may be able to finally resolve the question of asymptotic Nu scaling in turbulent convection.

Acknowledgements

After this manuscript was written our senior author, Charles Doering, passed away too soon. Beyond his many contributions to the present study, we are forever indebted to him for his mentorship, to say nothing of his many lasting contributions to the field of fluid dynamics. He will be deeply missed by us and many others. We also want to acknowledge helpful discussions about the present work with L.M. Smith, D. Sondak, and F. Waleffe. This work was supported by US National Science Foundation awards (DMS-1515161, DMS-1813003), Canadian NSERC Discovery Grants Program awards (RGPIN-2018-04263, RGPAS-2018-522657, DGEGR-2018-00371), and computational resources provided by Advanced Research Computing at the University of Michigan.

Declaration of interests

The authors report no conflict of interest.

Supplementary Material*Numerical solutions*

Tables 1S to 3S give the Nu , k , and Re values for numerical solutions with $Pr = 1$ and $\Gamma = 2$, Γ^* , and Γ_{loc}^* , respectively.

Table 1S: Details for numerical solutions with $Pr = 1$ and $\Gamma = 2$, including the resolution of Fourier modes (N_x) and Chebyshev collocation points (N_z).

Ra	Pr	$k = 2\pi/\Gamma$	$N_x \times N_z$	Nu	Re
$10^{13/4}$	1	π	128×65	1.056590	1.617336
1.9×10^3	1	π	128×65	1.145807	2.682155
2×10^3	1	π	128×65	1.212037	3.317190
2.25×10^3	1	π	128×65	1.355410	4.550975
2.5×10^3	1	π	128×65	1.474455	5.537770
2.75×10^3	1	π	128×65	1.575599	6.391812
3×10^3	1	π	128×65	1.663162	7.159844
$10^{14/4}$	1	π	128×65	1.714193	7.624400
3.5×10^3	1	π	128×65	1.808754	8.526064
4×10^3	1	π	128×65	1.926775	9.740578
4.5×10^3	1	π	128×65	2.025985	10.85141
5×10^3	1	π	128×65	2.111714	11.88534
$10^{15/4}$	1	π	128×65	2.204811	13.09152
8×10^3	1	π	128×65	2.476330	17.05494
10^4	1	π	128×65	2.648664	20.07400
$10^{17/4}$	1	π	128×65	3.122843	29.50047
$10^{18/4}$	1	π	128×65	3.665041	42.29585
$10^{19/4}$	1	π	128×65	4.287042	59.56858
10^5	1	π	128×65	4.994322	82.84462
$10^{21/4}$	1	π	128×65	5.795869	114.2355
$10^{22/4}$	1	π	128×97	6.703915	156.5252
$10^{23/4}$	1	π	128×97	7.732236	213.4031
10^6	1	π	128×97	8.896615	289.7982
$10^{25/4}$	1	π	256×97	10.21546	392.2837
$10^{26/4}$	1	π	256×129	11.71065	529.6372
$10^{27/4}$	1	π	256×129	13.40898	713.6005
10^7	1	π	512×129	15.34493	959.9367
1.35×10^7	1	π	512×129	16.46456	1119.932
1.5×10^7	1	π	512×129	16.87881	1182.172
1.6×10^7	1	π	512×193	17.13944	1222.005
1.65×10^7	1	π	512×193	17.26636	1241.484
1.7×10^7	1	π	512×193	17.39216	1260.709
1.736×10^7	1	π	512×193	17.48282	1274.414
1.76×10^7	1	π	512×193	17.54351	1283.493
$10^{29/4}$	1	π	512×193	17.58987	1290.377
1.786×10^7	1	π	512×193	17.60946	1293.277
1.8×10^7	1	π	512×193	17.64500	1298.522
1.85×10^7	1	π	512×193	17.77160	1317.122
1.9×10^7	1	π	512×193	17.89693	1335.501
1.95×10^7	1	π	512×193	18.02044	1353.657
2×10^7	1	π	512×193	18.14193	1371.593

2.4×10^7	1	π	512×193	19.04221	1507.890
2.8×10^7	1	π	512×193	19.83413	1633.418
$10^{30/4}$	1	π	512×193	20.47798	1739.647
4.5×10^7	1	π	512×193	22.44036	2087.182
$10^{31/4}$	1	π	512×193	23.76002	2340.822
10^8	1	π	768×257	27.50669	3144.931
$10^{33/4}$	1	π	768×257	31.81154	4220.616
2.15×10^8	1	π	768×257	33.36657	4649.541
$10^{34/4}$	1	π	768×257	36.75427	5658.648
4.64×10^8	1	π	896×321	40.44652	6875.704
$10^{35/4}$	1	π	896×321	42.42917	7580.057
10^9	1	π	1024×321	48.94284	10145.79
$10^{37/4}$	1	π	1024×321	56.42926	13571.10
2.15×10^9	1	π	1024×321	59.13988	14935.81
2.5×10^9	1	π	1024×321	61.38714	16116.94
$10^{38/4}$	1	π	1024×321	65.06338	18145.61
$10^{153/16}$	1	π	1024×321	67.42466	19511.79
4×10^9	1	π	1024×321	68.96487	20429.24
4.64×10^9	1	π	1024×321	71.58241	22019.93
$10^{39/4}$	1	π	1024×321	75.09725	24262.22
10^{10}	1	π	1024×321	86.68318	32430.06
$10^{41/4}$	1	π	1024×321	100.0909	43339.02
2×10^{10}	1	π	1024×321	103.0738	45995.60
2.15×10^{10}	1	π	1024×321	104.9517	47705.08

Table 2S: Details for numerical solutions with $Pr = 1$ and the aspect ratios Γ^* that globally maximize $Nu(\Gamma)$, including the resolution of Fourier modes (N_x) and Chebyshev collocation points (N_z).

Ra	Pr	$k = 2\pi/\Gamma^*$	$N_x \times N_z$	Nu	Re
$10^{13/4}$	1	3.116683	128×65	1.056697	1.619793
1.9×10^3	1	3.123537	128×65	1.145870	2.683859
2×10^3	1	3.128360	128×65	1.212070	3.318462
2.25×10^3	1	3.143491	128×65	1.355411	4.550777
2.5×10^3	1	3.161280	128×65	1.474516	5.535574
2.75×10^3	1	3.180831	128×65	1.575828	6.387203
3×10^3	1	3.202416	128×65	1.663668	7.152347
$10^{14/4}$	1	3.216383	128×65	1.714937	7.614958
3.5×10^3	1	3.247094	128×65	1.810118	8.512058
4×10^3	1	3.292192	128×65	1.929322	9.719380
4.5×10^3	1	3.329096	128×65	2.029942	10.82473
5×10^3	1	3.378413	128×65	2.117243	11.84892
$10^{15/4}$	1	3.426419	128×65	2.212421	13.04623
8×10^3	1	3.575467	128×65	2.492199	17.05494
10^4	1	3.665236	128×65	2.671348	19.99537
$10^{17/4}$	1	3.880392	128×65	3.171063	29.49222
$10^{18/4}$	1	4.118841	128×65	3.757873	42.57254
$10^{19/4}$	1	4.419469	128×89	4.454688	60.44520
10^5	1	4.793529	128×89	5.278963	84.69567
$10^{21/4}$	1	5.242992	128×129	6.252782	117.4323

$10^{22/4}$	1	5.782949	128×129	7.404680	161.3367
$10^{23/4}$	1	6.420133	128×129	8.769978	219.8304
10^6	1	7.171170	128×129	10.39171	297.1691
$10^{25/4}$	1	8.051634	128×129	12.32188	398.7272
$10^{26/4}$	1	9.073939	128×129	14.62274	531.4357
5×10^6	1	9.997275	192×257	16.76769	665.2339
$10^{27/4}$	1	10.25059	192×257	17.36827	704.3108
10^7	1	11.59439	192×257	20.64616	929.1624
$10^{29/4}$	1	13.12083	192×257	24.56044	1221.405
3×10^7	1	14.68186	256×257	28.77198	1562.064
$10^{30/4}$	1	14.84741	256×257	29.23512	1601.174
$10^{31/4}$	1	16.80072	256×257	34.81847	2094.287
10^8	1	18.99815	256×321	41.48855	2735.227
$10^{33/4}$	1	21.45545	256×321	49.46027	3569.756
3×10^8	1	23.89666	256×321	58.05030	4550.127
$10^{34/4}$	1	24.15059	256×321	58.99612	4663.393
$10^{35/4}$	1	26.84021	256×321	70.43089	6139.224
6×10^8	1	27.08270	256×321	71.85714	6344.418
6.5×10^8	1	27.31152	256×321	73.66207	6619.142
7×10^8	1	27.35757	256×321	75.37932	6911.933
7.5×10^8	1	26.83143	256×321	77.02411	7294.891
8×10^8	1	26.28179	256×321	78.61210	7683.031
8.5×10^8	1	26.25586	256×321	80.14209	7971.925
9×10^8	1	26.36825	256×321	81.61573	8227.378
9.5×10^8	1	26.54403	256×321	83.03697	8462.830
10^9	1	26.73696	256×321	84.40976	8687.394
$10^{37/4}$	1	29.78702	512×449	101.5246	11462.12
$10^{38/4}$	1	33.65968	512×449	122.1559	14978.49
$10^{39/4}$	1	38.04901	512×449	146.9986	19554.08
10^{10}	1	42.83017	512×449	176.9293	25585.09
$10^{41/4}$	1	48.06231	512×449	213.0247	33536.66
$10^{42/4}$	1	53.90331	512×449	256.5802	43967.29
$10^{43/4}$	1	60.50367	512×513	309.1454	57597.49
10^{11}	1	67.95755	512×513	372.5844	75402.24
$10^{45/4}$	1	76.33729	512×769	449.1508	98685.64
$10^{46/4}$	1	85.71701	512×897	541.5753	129175.9
$10^{47/4}$	1	96.12138	512×897	653.1727	169237.3
10^{12}	1	107.6085	512×897	787.9764	221995.2
$10^{49/4}$	1	120.1234	512×897	950.9070	291852.5
$10^{50/4}$	1	133.7508	512×897	1147.971	384498.9
$10^{51/4}$	1	148.8836	512×1025	1386.450	506738.9
10^{13}	1	166.3042	512×1025	1675.036	666086.2
$10^{53/4}$	1	186.3974	512×1025	2024.094	873176.4
$10^{54/4}$	1	209.4395	512×1281	2446.172	1142290
$10^{55/4}$	1	235.2120	512×1537	2956.470	1494811
10^{14}	1	263.0987	512×1793	3573.640	1962459

Table 3S: Details for numerical solutions with $Pr = 1$ and the aspect ratios Γ_{loc}^* that locally maximize $Nu(\Gamma)$, including the resolution of Fourier modes (N_x) and Chebyshev collocation points (N_z).

Ra	Pr	$k = 2\pi/\Gamma_{loc}^*$	$N_x \times N_z$	Nu	Re
$10^{22/4}$	1	14.09456	96×129	5.864201	82.92705
$10^{23/4}$	1	16.41959	96×129	6.914669	105.6969
10^6	1	18.89401	96×129	8.148261	135.6083
$10^{25/4}$	1	21.66773	96×129	9.587445	173.8004
$10^{26/4}$	1	24.88046	96×129	11.26803	221.7384
5×10^6	1	27.86575	96×129	12.81012	267.8677
$10^{27/4}$	1	28.70377	96×129	13.23878	280.9653
10^7	1	33.19466	96×129	15.56038	354.6158
$10^{29/4}$	1	38.29704	96×129	18.29931	448.0501
3×10^7	1	43.50700	96×193	21.21050	554.8653
$10^{30/4}$	1	44.06680	96×193	21.52859	566.9565
$10^{31/4}$	1	50.67686	96×193	25.33533	717.1889
10^8	1	58.31124	96×193	29.82540	906.1212
$10^{33/4}$	1	67.11615	128×321	35.12519	1143.903
3×10^8	1	76.25123	128×321	40.76618	1413.329
$10^{34/4}$	1	77.23740	128×321	41.38311	1443.747
$10^{35/4}$	1	88.88239	128×321	48.77387	1821.661
10^9	1	102.3071	128×321	57.50461	2297.406
$10^{37/4}$	1	117.7822	128×449	67.82060	2896.298
$10^{38/4}$	1	135.6225	128×449	80.01178	3650.131
$10^{39/4}$	1	156.1963	128×449	94.42106	4598.740
10^{10}	1	179.9312	128×449	111.4542	5792.111
$10^{41/4}$	1	207.3119	128×449	131.5910	7293.324
$10^{42/4}$	1	238.9044	128×449	155.3995	9181.462
$10^{43/4}$	1	275.3612	128×449	183.5515	11555.93
10^{11}	1	317.4310	128×449	216.8420	14541.83
$10^{45/4}$	1	365.9813	128×641	256.2116	18296.30
$10^{46/4}$	1	422.0132	128×641	302.7737	23016.84
$10^{47/4}$	1	486.6804	128×641	357.8457	28951.78
10^{12}	1	561.6657	128×641	422.9866	36390.82
$10^{49/4}$	1	647.4534	128×641	500.0423	45793.62
$10^{50/4}$	1	746.8566	128×641	591.1965	57587.15
$10^{51/4}$	1	861.4431	128×769	699.0342	72424.84
10^{13}	1	994.2189	128×769	826.6155	91031.10
$10^{53/4}$	1	1147.050	128×769	977.5620	114458.7
$10^{54/4}$	1	1323.461	128×1025	1156.161	143907.6
$10^{55/4}$	1	1527.004	128×1025	1367.486	180935.2
10^{14}	1	1762.395	128×1025	1617.546	227422.7

Comparison with turbulent convection

Figure 1S is nearly identical to figure 5 in the main text, comparing heat transport by Nu -maximizing steady rolls with transport by turbulent convection, except that more experimental data with Prandtl numbers further from 1 are included. In figure 1S the

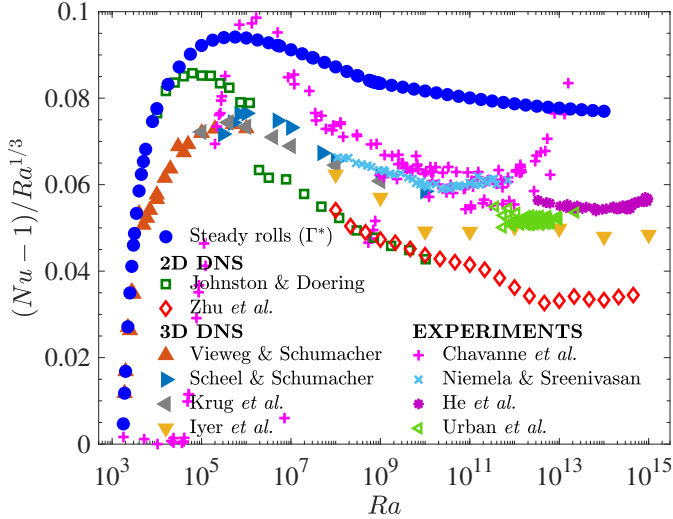


Figure 1S. Nu compensated by $Ra^{1/3}$ for steady rolls of Nu -maximizing aspect ratios Γ^* at $Pr = 1$, along with Nu from turbulent 2D and 3D DNS and experiments with estimated $Pr \in [0.6, 2]$. For horizontally periodic domains, 2D DNS with $(\Gamma, Pr) = (2, 1)$ were done by Johnston & Doering (2009) and Zhu *et al.* (2018), and 3D DNS with $\Gamma \geq 8$ and $Pr = 1$ were done by Vieweg & Schumacher (2020) and Krug *et al.* (2020). For DNS in cylinders of diameter-to-height ratio Γ_c , Iyer *et al.* (2020) used $(\Gamma_c, Pr) = (0.1, 1)$ and Scheel & Schumacher (2017) used $(\Gamma_c, Pr) = (1, 0.7)$. For laboratory experiments in cylinders, where the plotted data is truncated according to $Pr \in [0.5, 2]$, the domains and estimated Pr ranges are $\Gamma_c = 0.5$ and $Pr \in [0.6, 2]$ for Chavanne *et al.* (2001), $\Gamma_c = 4$ and $Pr \in [0.69, 1.84]$ for Niemela & Sreenivasan (2006), $\Gamma_c = 0.5$ and $Pr \in [0.79, 0.86]$ for He *et al.* (2012), and $\Gamma_c = 1$ and $Pr \in [0.95, 1.5]$ for Urban *et al.* (2014). Experiments used working fluids of low-temperature helium gas (Chavanne *et al.* 2001; Niemela & Sreenivasan 2006; Urban *et al.* 2014) or sulfur hexafluoride (He *et al.* 2012).

criterion for inclusion is an estimated Prandtl number of $Pr \in [0.5, 2]$ rather than the range $Pr \in [0.7, 1.3]$ in figure 5 of the main text. (In fact all of the estimated Pr are at least 0.6, so $Pr \in [0.6, 2]$ in figure 1S.) The working fluids in the experiments—gaseous helium or sulfur hexafluoride—are used near their critical points, leading to coupling and sensitive variation of material parameters that can be difficult to estimate. Faster variation of Pr with Ra is associated with increasing non-Oberbeck–Boussinesq effects as well; see Urban *et al.* (2011, 2012, 2014) for a discussion of experimental challenges. Data in figure 5 is truncated using the narrower range $Pr \in [0.7, 1.3]$ mainly to reduce non-Oberbeck–Boussinesq effects—we expect Pr alone to have a more modest effect, even over the wider range $[0.5, 2]$.

REFERENCES

- CHAVANNE, X., CHILLA, F., CHABAUD, B., CASTAING, B. & HEBRAL, B. 2001 Turbulent Rayleigh–Bénard convection in gaseous and liquid He. *Physics of Fluids* **13**, 1300–1320.
- CHILLÀ, F. & SCHUMACHER, J. 2012 New perspectives in turbulent Rayleigh–Bénard convection. *The European Physical Journal E* **35**, 58.
- CHINI, G.P. & COX, S.M. 2009 Large Rayleigh number thermal convection: Heat flux predictions and strongly nonlinear solutions. *Physics of Fluids* **21**, 083603.
- DOERING, C.R. 2020 Turning up the heat in turbulent thermal convection. *Proceedings of the National Academy of Sciences USA* **117**, 9671–9673.
- DOERING, C.R. & CONSTANTIN, P. 1996 Variational bounds on energy dissipation in incompressible flows. III. Convection. *Phys. Rev. E* **53**, 5957–5981.
- DOERING, C.R., OTTO, F. & REZNIKOFF, M.G. 2006 Bounds on vertical heat transport for infinite-Prandtl-number Rayleigh–Bénard convection. *J. Fluid Mech.* **560**, 229–241.
- GIBSON, J.F., HALCROW, J. & CVITANOVIĆ, P. 2008 Visualizing the geometry of state space in plane Couette flow. *Journal of Fluid Mechanics* **611**, 107–130.
- GRAHAM, M.D. & FLORYAN, D. 2021 Exact coherent states and the nonlinear dynamics of wall-bounded turbulent flows. *Annual Review of Fluid Mechanics* **53**, 227–253.
- HE, X., FUNFSCHILLING, D., NOBACH, H., BODENSCHATZ, E. & AHLERS, G. 2012 Transition to the ultimate state of turbulent Rayleigh–Bénard convection. *Physical Review Letters* **108**, 024502.
- HOWARD, L.N. 1963 Heat transport by turbulent convection. *Journal of Fluid Mechanics* **17**, 405–432.
- IYER, K.P., SCHEEL, J.D., SCHUMACHER, J. & SREENIVASAN, K.R. 2020 Classical $1/3$ scaling of convection holds up to $Ra = 10^{15}$. *Proceedings of the National Academy of Sciences USA* **117**, 7594–7598.
- JEFFREYS, H. 1928 Some cases of instability in fluid motion. *Proceedings of the Royal Society A* **118**, 195–208.
- JOHNSTON, H. & DOERING, C.R. 2009 Comparison of turbulent thermal convection between conditions of constant temperature and constant flux. *Physical Review Letters* **102**, 064501.
- KADANOFF, L.P. 2001 Turbulent heat flow: Structures and scaling. *Physics Today* **54**, 34–39.
- KOOLOTH, P., SONDAK, D. & SMITH, L.M. 2021 Coherent solutions and transition to turbulence in two-dimensional Rayleigh–Bénard convection. *Phys. Rev. Fluids* **6**, 013501.
- KRUG, D., LOHSE, D. & STEVENS, R.J.A.M. 2020 Coherence of temperature and velocity superstructures in turbulent Rayleigh–Bénard flow. *J. Fluid Mech.* **887**, A2.
- MOTOKI, S., KAWAHARA, G. & SHIMIZU, M. 2021 Multi-scale steady solution for Rayleigh–Bénard convection. *Journal of Fluid Mechanics* **914**, A14.
- NAGATA, M. 1990 Three-dimensional finite-amplitude solutions in plane couette flow: bifurcation from infinity. *Journal of Fluid Mechanics* **217**, 519–527.
- NIEMELA, J.J. & SREENIVASAN, K.R. 2006 Turbulent convection at high Rayleigh numbers and aspect ratio 4. *Journal of Fluid Mechanics* **557**, 411–422.
- OLSON, M.L., GOLUSKIN, D., SCHULTZ, W.W. & DOERING, C.R. 2021 Heat transport bounds for a truncated model of Rayleigh–Bénard convection via polynomial optimization. *Physica D* **415**, 132748.
- OTTO, F. & SEIS, C. 2011 Rayleigh–Bénard convection: Improved bounds on the Nusselt number. *J. Math. Phys.* **52**, 083702.
- RAYLEIGH, LORD 1916 On convection currents in a horizontal layer of fluid, when the higher temperature is on the under side. *Philosophical Magazine* **32**, 529–546.
- SCHEEL, J.D. & SCHUMACHER, J. 2017 Predicting transition ranges to fully turbulent viscous boundary layers in low Prandtl number convection flows. *Physical Review Fluids* **2**, 123501.
- SONDAK, D., SMITH, L.M. & WALEFFE, F. 2015 Optimal heat transport solutions for Rayleigh–Bénard convection. *Journal of Fluid Mechanics* **784**, 565–595.
- SURI, B., KAGEORGE, L., GRIGORIEV, R.O. & SCHATZ, M.F. 2020 Capturing turbulent dynamics and statistics in experiments with unstable periodic orbits. *Physical Review Letters* **125**, 064501.

- TREFETHEN, L.N. 2000 *Spectral Methods in MATLAB*. SIAM.
- URBAN, P., HANZELKA, P., KRÁLIK, T., MUSILOVA, V. & SRNKA, A. AND SKRBEK, L. 2012 Effect of boundary layers asymmetry on heat transfer efficiency in turbulent Rayleigh–Bénard convection at very high Rayleigh numbers. *Physical Review Letters* **109**, 154301.
- URBAN, P., HANZELKA, P., MUSILOVÁ, V., KRÁLÍK, T., LA MANTIA, M., SRNKA, A. & SKRBEK, L. 2014 Heat transfer in cryogenic helium gas by turbulent Rayleigh–Bénard convection in a cylindrical cell of aspect ratio 1. *New Journal of Physics* **16**, 053042.
- URBAN, P., MUSILOVÁ, V. & SKRBEK, L. 2011 Efficiency of heat transfer in turbulent Rayleigh–Bénard convection. *Physical Review Letters* **107**, 014302.
- VIEWEG, P. & SCHUMACHER, J. 2020 From 3D DNS with $Pr = 1$ and $\Gamma \geq 8$ by P. Vieweg and J. Schumacher. Private Communication.
- WALEFFE, F. 1998 Three-dimensional coherent states in plane shear flows. *Physical Review Letters* **81**, 4140.
- WALEFFE, F. 2020 Cases with the 6 largest $Ra \leq 10^9$ are from computations of F. Waleffe. Private Communication.
- WALEFFE, F., BOONKASAME, A. & SMITH, L.M. 2015 Heat transport by coherent Rayleigh–Bénard convection. *Physics of Fluids* **27**, 051702.
- WEDIN, H. & KERSWELL, R.R. 2004 Exact coherent structures in pipe flow: travelling wave solutions. *Journal of Fluid Mechanics* **508**, 333–371.
- WEN, B. & CHINI, G.P. 2018 Inclined porous medium convection at large Rayleigh number. *Journal of Fluid Mechanics* **837**, 670–702.
- WEN, B., CORSON, L.T. & CHINI, G.P. 2015 Structure and stability of steady porous medium convection at large Rayleigh number. *Journal of Fluid Mechanics* **772**, 197–224.
- WEN, B., GOLUSKIN, D., LEDUC, M., CHINI, G.P. & DOERING, C.R. 2020 Steady Rayleigh–Bénard convection between stress-free boundaries. *Journal of Fluid Mechanics* **905**, R4.
- WHITEHEAD, J.P. & DOERING, C.R. 2011 Ultimate state of two-dimensional Rayleigh–Bénard convection between free-slip fixed-temperature boundaries. *Phys. Rev. Lett.* **106**, 244501.
- WHITEHEAD, J.P. & DOERING, C.R. 2012 Rigid bounds on heat transport by a fluid between slippery boundaries. *J. Fluid Mech.* **707**, 241–259.
- ZHU, X., MATHAI, V., STEVENS, R.J.A.M., VERZICCO, R. & LOHSE, D. 2018 Transition to the ultimate regime in two-dimensional Rayleigh–Bénard convection. *Physical Review Letters* **120**, 144502.